



Effect of Water Vapor on Lifetime of 625 and 120 Foils During Oxidation Between 650 and 800 °C

M. Romedenne¹ · R. Pillai¹ · S. Dryepondt¹ · B. A. Pint¹

Received: 5 February 2021 / Revised: 7 June 2021 / Accepted: 27 June 2021 /

Published online: 29 July 2021

© The Author(s), under exclusive licence to Springer Science+Business Media, LLC, part of Springer Nature 2021

Abstract

The oxidation behavior of alloy 625 and 120 foils was studied at 650, 700 and 800 °C in dry air and flowing air + 10% H₂O up to 10,000 h (alloy 625) or 30,000 h (alloy 120). The effect of water vapor on Cr loss was investigated. Manganese and iron in the 120 foil induced faster Cr depletion in the foil and breakdown of the Cr₂O₃ scale into Fe and Cr-rich oxide compared to the alloy 625 foil. In the latter case, the presence of Nb led to the formation of Nb and Cr-rich oxide after breakdown of the Cr₂O₃ scale. Simultaneous Cr loss due to oxidation and volatilization of the Cr₂O₃ oxide scale was predicted and compared to experimental Cr loss measurements for exposures up to 30,000 h.

Keywords Foil oxidation · Lifetime · Modeling · Water vapor · Microturbine

Introduction

To improve efficiency of advanced recuperators, temperatures above 600 °C are required [1, 2]. At $T > 600^\circ\text{C}$, the commonly used Fe-based austenitic alloys (such as 347: Fe–10Ni–18Cr) cannot be employed due to their reduced oxidation lifetime in water vapor containing microturbine exhaust [2–5]. Over the past few decades,

This manuscript has been authored by UT-Battelle, LLC under Contract No. DE-AC05-00OR22725 with the U.S. Department of Energy. The United States Government retains and the publisher, by accepting the article for publication, acknowledges that the United States Government retains a non-exclusive, paid-up, irrevocable, world-wide license to publish or reproduce the published form of this manuscript, or allow others to do so, for United States Government purposes. The Department of Energy will provide public access to these results of federally sponsored research in accordance with the DOE Public Access Plan (<http://energy.gov/downloads/doe-public-access-plan>).

✉ M. Romedenne
romedennem@ornl.gov

¹ Materials Science and Technology Division, Oak Ridge National Laboratory, Oak Ridge, TN 37831-6156, USA

significant research effort has been directed towards evaluating and understanding the combined effect of water vapor and increased temperature on the long-term oxidation behavior of ferritic steels [6, 7], austenitic Ni–Fe-based alloys [3, 8–13] and superalloys [14, 15] in air and water vapor. In O₂–H₂O mixtures with high H₂O/O₂ ratio, for temperatures between 550 and 650 °C, ferritic steels, such as Fe–9–12Cr–1Mo, rapidly formed thick and non-protective Fe-rich oxide scales [6, 7]. Regarding austenitic Ni–Fe-based alloys, the volatilization of the external Cr₂O₃ oxide scale into CrO₂(OH)₂ [16, 17] accelerated Cr depletion in the 304L steel (2 mm thick coupon) after 679 h in flowing O₂ + 10% H₂O (100 mL min⁻¹ / 2.5 cm s⁻¹) at 600 °C in comparison with dry air [8]. After prolonged exposure, accelerated Cr depletion in Fe–20Cr–25Ni and Fe–20Cr–20Ni led to the formation of localized Fe-rich nodule formation, especially in the case of Fe-based foils exposed up to 10,000 h in flowing air + 10% H₂O (1.6–2.0 cm s⁻¹) at 650 and 700 °C [3, 10–12]. For Ni–30Cr–10Fe 1 mm coupon (alloy 690), breakdown of the Cr₂O₃ scale into Fe, Ni-rich oxide was observed after 200 h exposure in flowing air + 20% H₂O (31.6 cm s⁻¹) at 800 °C [13]. For 300 μm thick alloy 625 foil, the increased Cr depletion led to breakdown of Cr₂O₃ into NbCrO₄ after 1000 h in flowing air + 6% H₂O (0.5–600 cm s⁻¹) [14].

A solely experimental approach to evaluate the combined effect of weight gain (oxidation rate constant k_p) and weight loss (Cr₂O₃ volatilization rate constant k_{ev}) on Cr consumption over application relevant lifetimes (> 50,000 h) can be costly and time-consuming. Models to predict the influence of time, temperature, environments and flow rates on the oxidation induced lifetime of recuperator materials could significantly reduce the experimental effort in finding the appropriate alloy or foil and enable a detailed evaluation of the test variables. In particular, accurate validation of these models with long-term experimental data will allow rapid evaluation of microturbine components oxidation lifetime [18]. One purpose of the current work is to inform about modeling efforts with relevant experimental results.

Modeling of the Cr loss of materials in a wet environment was attempted by several authors [11, 14, 19–21]. Modeling of the oxidation and volatilization of Cr₂O₃ was first treated by Tedmon [19] for pure Cr or Fe–Cr alloys at 1000 °C where the CrO₃(g) was the main reaction product of Cr₂O₃ volatilization. At lower temperatures where CrO₂(OH)₂ was found predominant [16, 17, 22], the evaporation constant, k_{ev} , was expressed as function of mass transfer parameters [11, 20, 21]. Calculated Cr loss solely due to volatilization was higher than the measured Cr loss for alloy 709 foils exposed for 6000 h in flowing air + 10% H₂O (1.9 cm.s⁻¹) at 800 °C [11] and for alloy 625 foils oxidized for 1000 h in flowing air + 6% H₂O (70 and 600 cm.s⁻¹) at 900 °C [14]. Good agreement was obtained between the calculated k_{ev} and the experimental slope of the mass change data of alloys 230 and 625 exposed for 2000 h in flowing air + 37–38% H₂O (gas velocities of 0.19 and 0.76 cm.s⁻¹) at 760 °C [20] and 304L stainless steel exposed for 679 h in flowing O₂ + 10% H₂O (2.5 cm.s⁻¹) at 600 °C [8, 20].

Different methods were employed to predict the extent of volatilization of the Cr₂O₃ scale in the abovementioned studies. In [11, 14], the combined Cr loss due to both oxidation and volatilization of the Cr₂O₃ scale was not considered and could lead to underestimation of the Cr loss. Studies relying on the evaluation of the k_{ev}

Table 1 Composition of studied alloys (in wt%) analyzed by inductively coupled plasma-optical emission spectrometry (ICP-OES) and combustion analysis for carbon

Composition	Fe	Ni	Cr	Mo	Al	Mn	Ti	Si	Nb	C
120	32.2	39.5	25.8	0.45	0.04	0.52	0.01	0.33	0.42	0.054
625	4.5	60.9	21.9	8.4	0.12	0.06	0.19	0.18	3.4	0.039

Table 2 Calculated velocities as function of temperature for gas flowing at $850 \text{ cm}^3 \text{ min}^{-1}$ in a 5.9 cm alumina tube

Temperature (°C)	Velocity (cm s ⁻¹)
650	1.60
700	1.69
800	1.87

from the mass change data are limited by the strictly para-linear oxidation behavior of the mass change data [23, 24]. As a consequence [23, 24], the Cr loss solely due to volatilization was predicted for only one alloy foil (alloy 230), whereas several Ni-based foils (alloys X, 230, 120 and 282) were exposed in flowing air + 10% H₂O between 760 and 871 °C (500 cm³.min⁻¹), 30 day cycles.

In this study, the combined oxidation and volatilization behavior of alloy 625 and 120 foils were evaluated in dry air and in flowing air + 10% H₂O (850 cm³ min⁻¹) at 650, 700 and 800 °C. Compositional effects (Cr and Mn losses) were characterized as a function of time and temperature and atmosphere. In addition, the capability of a model to predict the Cr losses due to the combined effect of oxidation and volatilization was evaluated.

Experimental Procedures

Foil specimens of Haynes® 120 ($82 \pm 2 \mu\text{m}$ thickness) and 625 ($100 \pm 7 \mu\text{m}$ thickness) (analyzed compositions in Table 1) alloys were oxidized in dry air in a resistively heated alumina tube (100 h-cycles) furnace and in alumina crucibles (500 h-cycles) inserted in a box furnace for up to 10,000 h at 650, 700 and 800 °C. The specimens were also exposed in a resistively heated alumina tube furnace (diameter of 5.9 cm) with flowing (850 cm³ min⁻¹) air + (10 ± 1) vol% H₂O(g) (henceforth noted in the text as wet air) in 100 h-cycles for up to 10,000 h for the alloy 625 and for up to 30,000 h for the alloy 120 at 650, 700 and 800 °C. The resulting gas velocities for the three temperatures are reported in Table 2. A detailed description of the experimental procedure is available in [12]. Specimens were exposed in their as-rolled surface finish (i.e., no surface polishing performed), the alloys grain sizes were reported in [3] and were 23 and 12 μm for alloys 120 and 625, respectively, and the specimen mass changes were measured using a Mettler–Toledo model AG245 or XP205 balance with an accuracy of ±0.04 mg.

Table 3 Mass transfer parameters for $\text{CrO}_2(\text{OH})_2$ in flowing air + 10% H_2O at 1 atm between 650 and 800 °C

Temperature (°C)	650	700	800
Kinematic viscosity ν ($\text{cm}^2 \text{s}^{-1}$)	1.01	1.17	1.38
Gas velocity: u (cm s^{-1})	1.60	1.69	1.87
Binary gas diffusion coefficient: D ($\text{cm}^2 \cdot \text{s}^{-1}$)	0.8	0.9	1
Reynolds number: Re	3.18	2.89	2.71
Schmidt number: Sc	1.26	1.30	1.38
Sherwood number: Sh	0.248	0.244	0.251

Table 4 $\text{CrO}_2(\text{OH})_2$ partial pressures considering either Opila et al. data [17] or Gindorf et al. data [16] with resulting volatilization rate at the studied temperatures

Temperature (°C)	650	700	800
Partial pressure $\text{CrO}_2(\text{OH})_2$: $p^{(i)}$ (bar) Opila et al. [17]	$1.14 \cdot 10^{-7}$	$1.63 \cdot 10^{-7}$	$3.01 \cdot 10^{-7}$
Partial pressure $\text{CrO}_2(\text{OH})_2$: $p^{(i)}$ (bar) Gindorf et al. [16]	$0.27 \cdot 10^{-7}$	$0.41 \cdot 10^{-7}$	$0.84 \cdot 10^{-7}$
J_{Cr} [17] ($\text{g cm}^{-2} \text{s}^{-1}$)	$4.00 \cdot 10^{-11}$	$5.88 \cdot 10^{-11}$	$1.08 \cdot 10^{-10}$
J_{Cr} [16] ($\text{g cm}^{-2} \text{s}^{-1}$)	$9.44 \cdot 10^{-12}$	$1.48 \cdot 10^{-11}$	$3.02 \cdot 10^{-11}$

After exposure, specimens were Cu plated and mounted in conductive epoxy for cross-sectional characterization including scanning electron microscopy (SEM) using TESCAN model MIRA3, energy dispersive X-ray spectroscopy (EDS) using EDAX Octane Elect Super Silicon Drift Detector and electron probe microanalysis (EPMA) using JEOL model 8200/8500.

Determination of Volatile Flux of Cr in the Presence of Water Vapor

In this study, the Cr loss of the specimens due to oxidation and volatilization was modeled assuming a flat plate geometry and laminar flow. Oxidation rate constants were determined using dry air exposures and the volatilization rate (J_{Cr}) was calculated according to Eq. 1 and values in Table 3 [11, 20]. Since different values of the $\text{CrO}_2(\text{OH})_2$ partial pressure were measured in the literature [16, 17], different J_{Cr} values were calculated and reported in Table 4.

$$J_{\text{Cr}} = 0.664 \frac{(p^{(i)} - p^{(0)})}{RT} (D^4 / \nu)^{1/6} (u/l)^{1/2} M_{\text{Cr}} \quad (1)$$

with,

- J_{Cr} , the Cr volatilization flux ($\text{g cm}^{-2} \cdot \text{s}^{-1}$)
- $p^{(i)}$, the partial pressure of $\text{CrO}_2(\text{OH})_2$ at the specimen's surface

- $p^{(0)}$, the partial pressure of $\text{CrO}_2(\text{OH})_2$ away from the specimen's surface, assumed to be zero
- R , the universal gas constant ($\text{J K}^{-1} \text{ mol}^{-1}$)
- T , the temperature (K)
- D , the binary gas diffusion coefficient ($\text{cm}^2 \text{ s}^{-1}$) from [11]
- ν , the kinematic viscosity ($\text{cm}^2 \text{ s}^{-1}$) from [11]
- u , the gas velocity (cm s^{-1})
- l , the specimen length (2 cm)
- M_{Cr} , the molar mass of Cr (g mol^{-1})

Parameters associated with the gas dynamics are defined in Eqs. 2 to 4

$$\text{Sh} = 0.332 \text{Re}^{1/2} \text{Sc}^{1/3} \quad (2)$$

$$\text{Re} = \frac{ul}{D} < 5 \times 10^5 \quad (3)$$

$$0.6 < \text{Sc} = \frac{\nu}{D} < 50 \quad (4)$$

where the terms are described and specified for 650, 700 and 800 °C in Table 3 [11, 20].

The total chromium loss (oxidation and volatilization) was calculated solving the para-linear oxidation behavior from Tedmon [19] described in [25] with a MATLAB partial differential equation solver [26]. The oxidation rate constants and J_{Cr} in Table 4 were used assuming the exclusive formation of Cr_2O_3 on the surface of the specimens. The oxidation rate constant value was also increased by a factor of two to evaluate the effect of an increased oxidation rate in a water vapor atmosphere on the total Cr loss [27]. The current modeling approach accounts for the oxidation and volatilization induced Cr loss. It does not account for transport processes in the alloy.

Results in Dry Air and Air + 10% H_2O Environments

Oxidation Kinetics

Figure 1 shows the mass change for alloys 625 (Fig. 1a) and 120 (Fig. 1b) specimens in 100 h-cycle or 500 h-cycle dry air (open symbols) and wet air (solid symbols) between 650 and 800 °C. In dry air, mass gains were observed at all temperatures for alloys 625 and 120 specimens at 650 and 700 °C. For alloy 120, specimens were tested in dry air at 800 °C in both 100 and 500 h cycles. Slight variations were observed between the 100 and 500 h cycle mass change data (Fig. 1b). Mass gain was observed during 10,000 h for the 500 h cycle specimen and slight mass losses

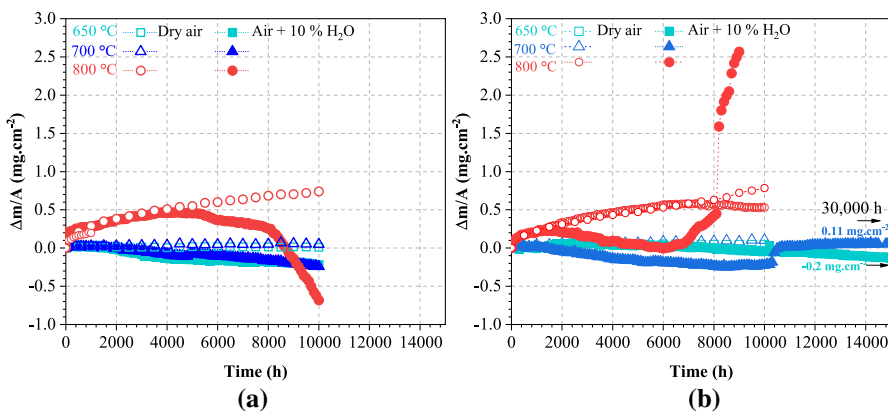


Fig. 1 **a** 625 and **b** 120 foil specimen mass change after 100h or 500h-cycle in (open symbols) dry air and (close symbols) air + 10% H₂O at 650, 700 and 800 °C

were seen after about 8000 h for the 100 h cycle specimen (Fig. 1b). Since the wet air exposures were done in 100 h cycles, characterizations from the 100 h cycle specimen in dry air at 800 °C are presented in the manuscript.

In wet air, alloy 625 specimens lost mass for the whole test duration (10,000 h) at 650 and 700 °C. At 800 °C, mass gain was measured up to 4000 h then followed by slight mass loss up to 9000 h and steeper mass loss between 9000 h and 10,000 h suggesting spallation of the oxide layer (Fig. 1a). For the 120 specimen, at 650 °C, mass gain was observed during the first 1000 h followed by mass loss for the remaining duration of the test (30,000 h in Fig. 1b). At 700 °C, mass loss was observed until 10,000 h where a slight increase in mass was measured and followed by steady-state mass gain until 30,000 h (0.11 mg.cm $^{-2}$ in Fig. 1b). At 800 °C, mass gain was measured up to 2000 h followed by mass loss until 6000 h. Afterwards, significant mass gain occurred, reaching 2.5 mg.cm $^{-2}$ for the alloy 120 after 9000 h exposure (Fig. 1b).

The oxidation rate constants (k_p) were determined from the steady-state mass change in dry air in Fig. 1 using Eq. 5, where Δm is the mass change in mg, A the surface area in cm 2 and t the time in h. The values are reported as a function of reciprocal temperature for 625 and 120 in Fig. 2. Larger standard deviations for k_p were measured at 650 and 700 °C than at 800 °C. The magnitude of the error bars was determined based on at least three mass change curves at each temperature. The k_p values were in agreement with literature values obtained between 900 and 1100 °C higher temperatures [28–32]

$$\left(\frac{\Delta m}{A} \right)^2 = k_p \times t \quad (5)$$

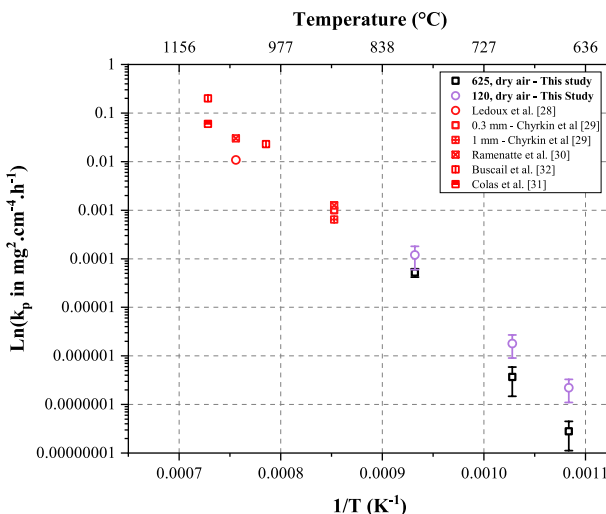


Fig. 2 Natural logarithm of oxidation rate constant calculated using the first 100 or 500 h data points in Fig. 1 in dry air at 650, 700 and 800 °C superimposed with literature values

Oxide Scale Nature and Evolution

General Remarks Unless otherwise stated in the text, results at 650 °C were similar to the 700 and 800 °C exposures, but with slower oxidation rates. For readability of the manuscript, most results will be presented at 700 and 800 °C.

Dry Air Atmosphere

In dry air, a Cr-rich oxide scale (Cr_2O_3) was formed on the surface of the 625 specimens for up to 10,000 h at 700 and 800 °C as shown in the SEM backscattered election (BSE) images (Figs. 3a and 4a). Al_2O_3 internal oxidation along the grain boundaries was also observed at 800 °C (Fig. 4a). The phase identifications were made using the EDS element maps at 700 °C (not shown here) and at 800 °C in Fig. 5a. The 625 specimens were constituted of austenite, δ Ni_3Nb precipitates and M_6C and/or $\text{M}_2\text{3C}_6$ carbides identified in the literature [29, 33] (Fig. 3a).

For the 120 specimens, the BSE images after 10,000 h exposure at 700 and 800 °C are reported in Figs. 3c and 4c. The elemental maps at 700 °C (not shown here) and at 800 °C (Fig. 5b) were used to identify the oxide layers. At 700 °C, for up to 10,000 h, Mn-rich spinel oxide (likely MnCr_2O_4) over a Cr-rich scale (likely Cr_2O_3) and Si-rich oxide particles (likely SiO_2) were formed at the alloy oxide interface for the 120 specimens (Fig. 3c). At 800 °C, the surface of the 120 specimen after 10,000 h exposure was mostly covered with Cr_2O_3 and MnCr_2O_4 oxide layers and SiO_2 underlying precipitates. In addition, Fe and Cr-rich oxide nodules were sparsely located along the surface (one nodule every $500 \pm 100 \mu$

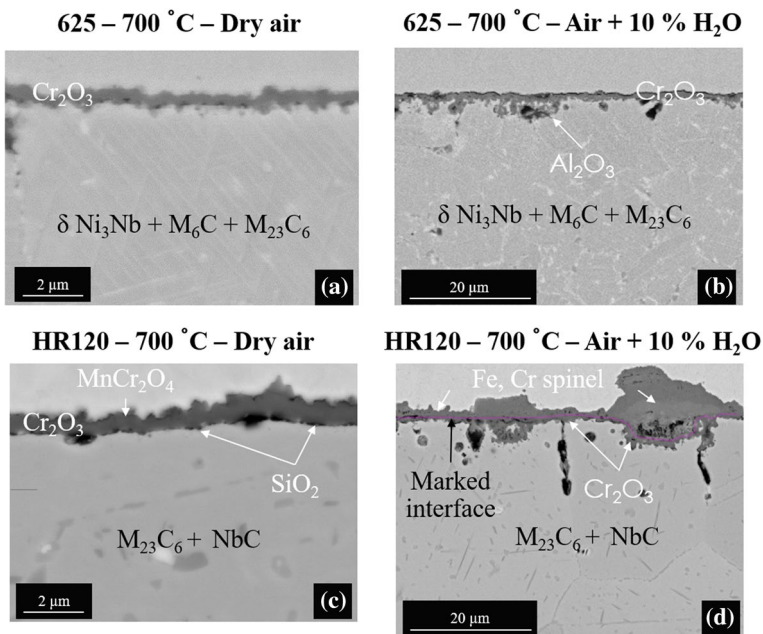


Fig. 3 SEM BSE images of specimen 625 after 10,000 h exposure in **a** 500 h-cycle dry air and **b** 100 h-cycle air + 10% H₂O at 700 °C and specimen 120 after 10,000 h exposure in **c** 500 h-cycle dry air and **d** 100 h-cycle air + 10% H₂O at 700 °C

m). The nodules were also formed at the corners of the foils (not shown here). These nodules were not observed after 5000 h exposure in dry air, but only after 10,000 h exposure as shown in Fig. 4c. After formation, the Fe and Cr mixed oxides were observed to have spalled at some locations after 10,000 h at 800 °C (Fig. 5b). The strengthening M₂₃C₆, NbC carbides and δ Ni₃Nb phase were identified based on the literature [33–35], see Fig. 3c.

Air + 10% H₂O atmosphere

For alloy 625, in wet air at 700 °C, the formation of Cr₂O₃ was sustained for 10,000 h based on the BSE image Fig. 3b and in EDS elemental maps Fig. 6a). At 800 °C, after 10,000 h, a Nb, Cr, Fe and Ni-rich oxide layer (henceforth named Nb, Cr mixed oxides, identification based solely on EDS data) about $9.5 \pm 5 \mu\text{m}$ thick was observed on one surface of the foil specimen (bottom of the BSE image in Fig. 4b). On the other surface of the specimen, a Cr₂O₃ scale and Al₂O₃ internal oxides are shown in the BSE image in Fig. 4b. The Nb-rich oxide was thicker (about 50 μm thick) on the corners of the foils as shown from the BSE image in Fig. 7 and EDS elemental maps in Fig. 8a. The evolution of the thickness of the Cr₂O₃ and Nb-rich oxide scales as a function of time is reported in Fig. 9a for both dry air and wet air atmospheres at 650, 700 and 800 °C. The formation of Cr₂O₃ was sustained 10,000 h in dry air at all temperatures. In wet air, Cr₂O₃ was replaced by the Nb-rich

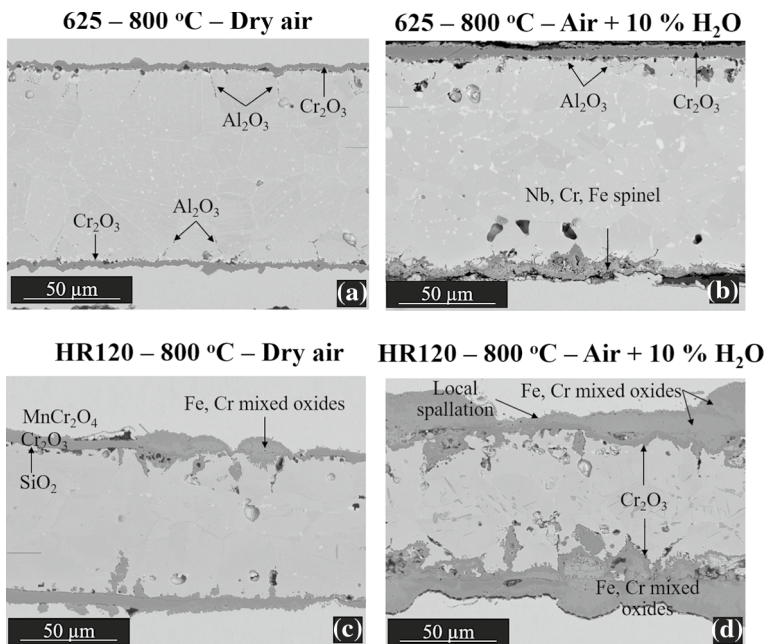


Fig. 4 SEM BSE images of specimen 625 after 10,000 h exposure in **a** 500 h-cycle dry air and **c** 100 h-cycle air + 10% H_2O at 800 °C and specimen 120 after 10,000 h exposure in **b** 100 h-cycle dry air and after **d** 9000 h exposure in 100 h-cycle air + 10% H_2O at 800 °C

oxide on one side of the specimen before 10,000 h exposure at 800 °C (star symbols in Fig. 9a).

For the 120 specimens, after 10,000 h exposure in wet air at 700 °C, the nature of the oxide scale was different than observed in dry air (BSE image in Fig. 3d and EDS elemental maps in Fig. 6b). As mentioned, in dry air, MnCr_2O_4 and Cr_2O_3 oxide layers were observed (Fig. 3c). In wet air, in most areas, the oxide layer consisted of a thick Fe, Cr-rich oxide layer (thickness of $1 \pm 0.2 \mu\text{m}$) on top of a thin Cr_2O_3 oxide layer (thickness of $1 \pm 0.2 \mu\text{m}$). At some locations, thicker oxide nodules ($5 \pm 2 \mu\text{m}$) (Fig. 3d) were observed. These nodules were mainly located above the grain boundaries of the alloy as seen above the Cr-depleted alloy grain boundaries (arrows in Fig. 6b). At 800 °C, after 9000 h exposure in wet air, a thicker Fe, Cr-rich oxide layer was observed ($19 \pm 5 \mu\text{m}$) (BSE image in Fig. 4 and EDS elemental maps in Fig. 8b). A Cr_2O_3 layer was observed underneath the oxide layer and was formed deeper along the grain boundaries of the alloy (Cr map in Fig. 8b). After formation, Fe and Cr mixed oxides were also found to have spalled (areas reported in Fig. 4d after 9500 h at 800 °C). The evolution of the nature and thickness of the oxide scale on the 120 specimen as a function of time is reported in Fig. 9b for each temperature. At 650 °C, the Fe and Cr-rich oxide layer was observed on top of the Cr_2O_3 after 1000 h and maintained for the whole duration of the experiment (30,000 h). At 700 °C, before 10,000 h exposure, the formation of Cr_2O_3 was observed (about $1.0 \pm 0.5 \mu\text{m}$ square symbols in Fig. 9b), after 10,000 h and up to

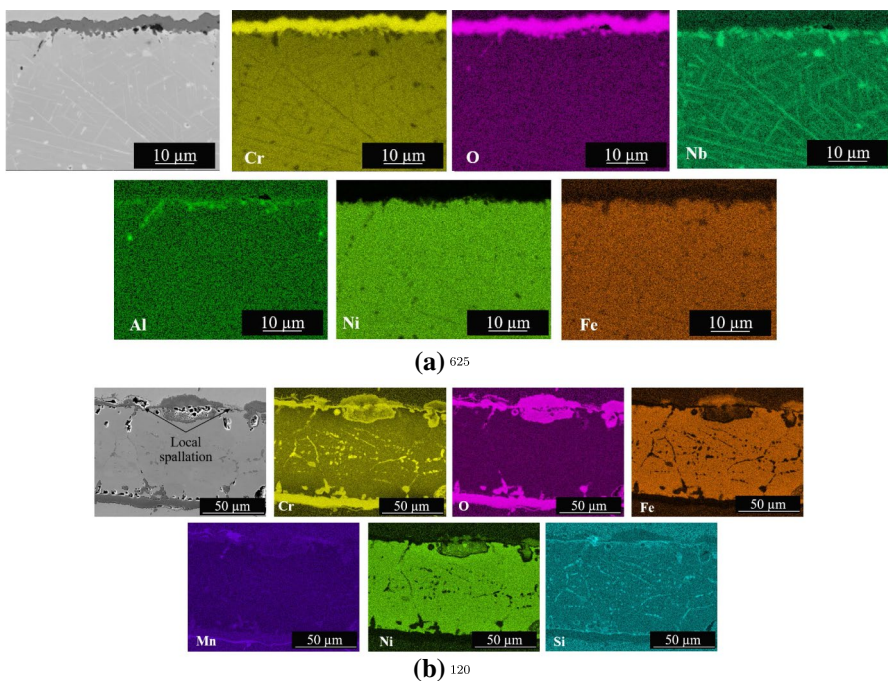


Fig. 5 SEM images and associated EDS quantified elemental maps of specimens **a** 625 specimen after 10,000 h exposure in 500 h-cycle dry air and **b** 120 specimen after 10,000 h exposure in 100 h-cycle dry air at 800 °C

30,000 h, the formation and growth of Cr_2O_3 was observed ($2.5 \pm 0.5 \mu\text{m}$) underneath the Fe, Cr-rich oxide layer and nodules. These nodules did not significantly grow between 10,000 h and 30,000 h ($5 \pm 2 \mu\text{m}$ thickness star symbols in Fig. 9b). At 800 °C, only a Cr_2O_3 scale was observed up to 5000 h. After longer exposure times and up to 9000 h an Fe, Cr-rich oxide layer was observed and grew from 7 to 20 μm between 5000 and 9000 h (star symbols in Fig. 9b). The growth of the mixed oxides was related to significant mass gain of the specimen in Fig. 1b. Therefore, the specimen was removed from the furnace before 10,000 h to limit its deformation and allow characterizations.

Compositional Changes in the Underlying Alloys

EDS elemental profiles were measured in the underlying 625 and 120 foils (Figs. 10 and 11). Because of the variations in the initial foil thicknesses between 625 and 120 foils, the post exposure foil thicknesses were normalized to their thickness measured before exposure. Therefore, the x-axis is reported in % in (Figs. 10 and 11). At least three Cr and Mn concentration profiles were measured in the matrix of each specimen at each condition. Between several profiles, a 5% relative error was observed. For example, for the 625 foil, the Cr concentration at the alloy-oxide interface varied

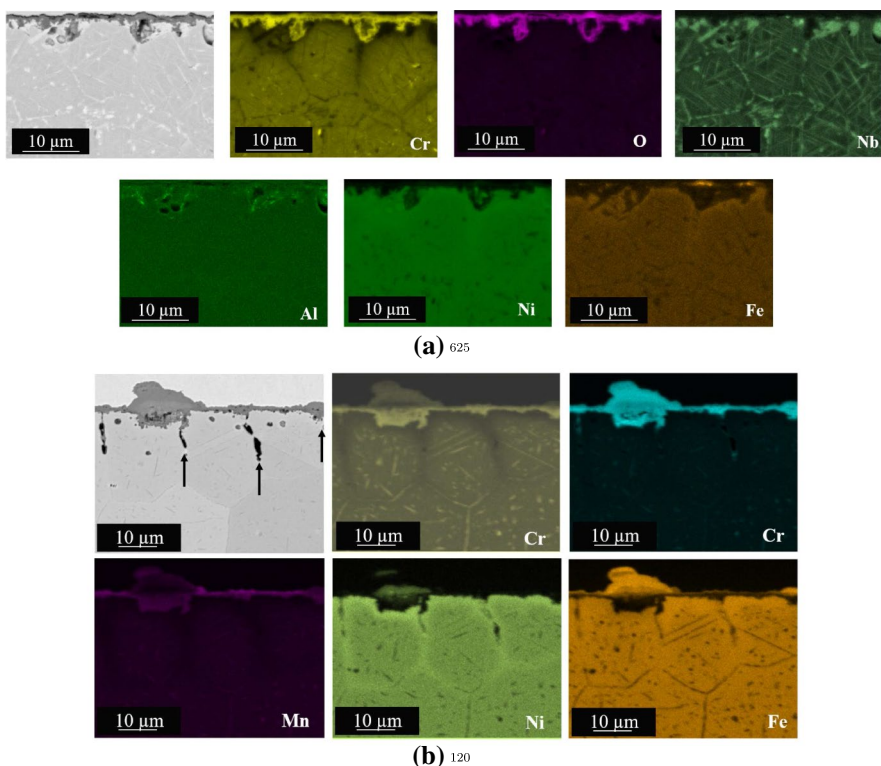
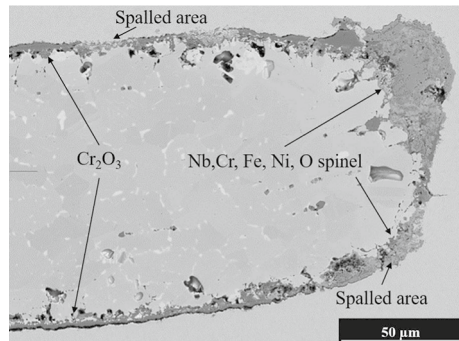


Fig. 6 SEM images and associated EDS elemental maps of **a** 625 and **b** 120 specimens after 10,000 h exposure in 100 h-cycle air + 10% H₂O at 700 °C

Fig. 7 BSE image of corner of specimen 625 after 10,000 h exposure in 100 h-cycle air + 10% H₂O at 800 °C



between 3 and 7 wt% as shown in Fig. 10a after 10,000 h exposure in wet air at 800 °C. From all the EDS Cr elemental profiles measured in the foils, the time to 10 wt% Cr (t_{10}) at the oxide-alloy interface was evaluated and is reported for each temperature and environment of exposure for 625 and 120 foils in Table 5. The t_{10} metric has been used in the literature as the time when the critical Cr content at the

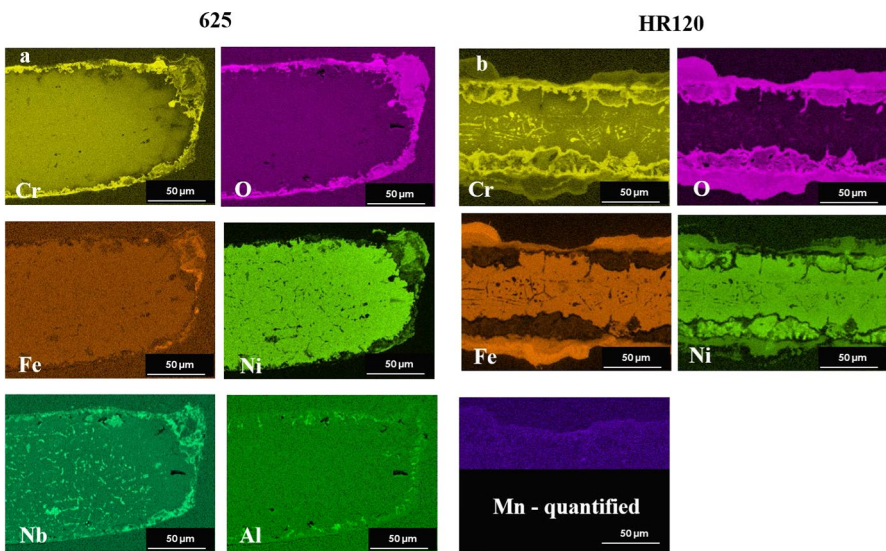


Fig. 8 SEM images and associated EDS quantified elemental maps of specimens **a** 625 after 10,000 h exposure in 100 h-cycle air + 10% H₂O and **b** 120 after 9000 h exposure in 100 h-cycle dry air + 10% H₂O at 800 °C

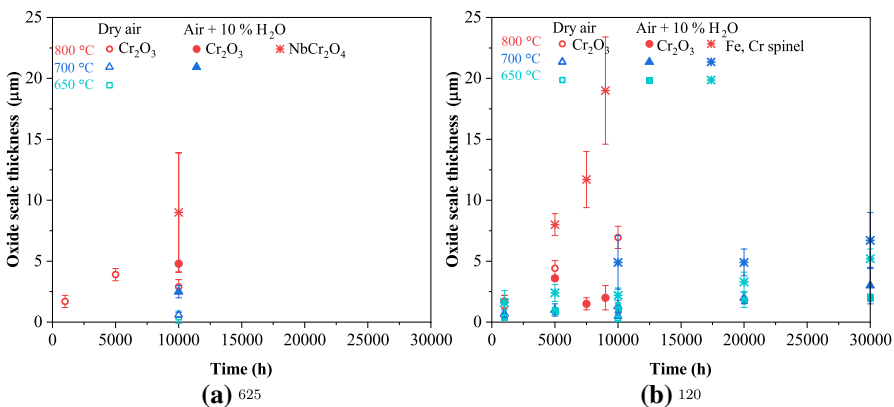


Fig. 9 **a** Thickness of the Cr₂O₃ (squares) and NbCr₂O₄ or Fe, Cr-rich oxide nodules (stars) measured on the cross sections of the **a** 625 and **b** 120 foils using image analysis after up to 30,000 h exposure in (open symbols) dry air and (closed symbols) air + 10% H₂O between 650 and 800 °C

metal-oxide interface, required to maintain Cr₂O₃ scale of Ni-based alloys, drops below 10 wt% [36–38]. This time is effectively the onset of Cr₂O₃ breakdown as indicated in the previous section by the formation of Nb, Cr mixed oxides on the 625 specimens and Fe, Cr, Ni mixed oxides on the 120 specimens.

For alloy 625, at 650 and 700 °C, t_{10} was not reached after 10,000 h in either the dry or wet air environments. At 800 °C, t_{10} was not reached in dry air but was reached

Table 5 Time to 10 wt% Cr (t_{10}) at the oxide-alloy interface in 625 and 120 foil specimens after exposure in dry air and air + 10% H₂O at 650, 700 and 800 °C

Tem- perature (°C)	625 (100–125 μm)—Dry air	625 (100–125 μm)— Air + 10% H ₂ O	120 (80–82 μm)—Dry air	120 (80–82 μm)—Air + 10% H ₂ O
650	10,000 h < t_{10}	10,000 h < t_{10}	10,000 h < t_{10}	$t_{10} < 1000$ h
700	10,000 h < t_{10}	10,000 h < t_{10}	10,000 h < t_{10}	5000 < $t_{10} < 10,000$ h
800	10,000 h < t_{10}	5000 < $t_{10} < 10,000$ h	Close to 10,000 h	5000 < $t_{10} < 7500$ h

Evaluated from the measured EDS-EPMA Cr elemental profiles in the foils

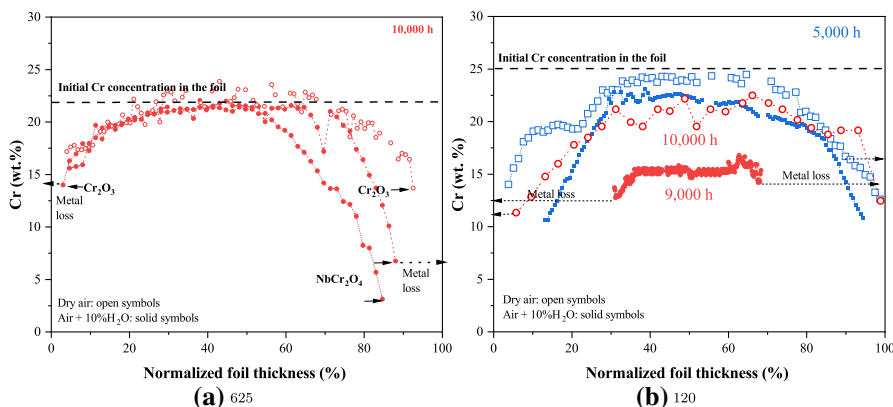
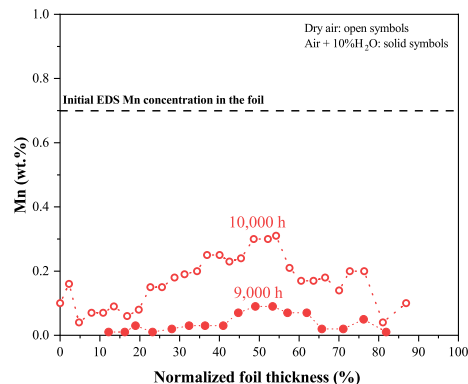


Fig. 10 EDS elemental Cr profiles measured in **a** 625 and **b** 120 foils after **a** 10,000 h exposure in (open symbols) dry air and (close symbols) air + 10% H₂O at 800 °C. **b** 5000 and 10,000 h exposure in (open symbols) dry air and (close symbols) after 5000 and 9000 h exposure in air + 10% H₂O at 800 °C. The metal loss, due to the formation of oxides on the surface of the specimens, is indicated with dashed arrows

Fig. 11 EDS elemental Mn profiles measured 120 foils after 10,000 h exposure in (open symbols) dry air and (close symbols) 9000 h in air + 10% H₂O at 800 °C



in wet air on one side of the specimen (Table 5 and solid symbols in Fig. 10a). In addition, after 10,000 h in wet air at 800 °C, the Cr depletion had reached the center

of the foil from one side of the specimen (Fig. 10a). This was in agreement with the observed formation of Nb and Cr-rich oxide under these conditions (BSE image in Fig. 4b and evolution of oxide thickness in Fig. 9a).

For alloy 120, in dry air, at 650, 700 °C and 800 °C t_{10} could not be measured after 10,000 h since the breakdown of the Cr_2O_3 scale occurred earlier. Indeed, after 5000 h at 800 °C, the Cr concentration at the alloy-oxide interface was close to 10 wt% correlated to the formation of Fe, Cr-rich nodules on the surface of the specimens (evolution of oxide thickness and nature in Fig. 9b). In addition, after 10,000 h, the foil was also Cr-depleted in the center (20 wt% instead of 25 wt% in Fig. 10b). Therefore, t_{10} was considered to be reached before 10,000 h in Table 5. In wet air at 650 °C, t_{10} was reached before 1000 h exposure (Cr profile not shown here). At 700 °C, it was reached between 5000 and 10,000 h and after 5000 to 7500 h at 800 °C (Table 5) (Cr profile not shown here). At 800 °C in wet air, the Cr concentration was close to 10 wt% after 5000 h of exposure and the Cr concentration in the center of the foil was lower (about 22 wt%) than its initial Cr concentration (25 wt%) (Cr profile in Fig. 10b). After 9000 h, an even larger Cr depletion was observed in the center of the foil (15 ± 1 wt% in Fig. 10b). Significant metal loss was also observed with only 40% of the metal thickness not being oxidized. These observations are in agreement with the thick Fe, Cr-rich oxide scale formed on the surface of the foil (EDS elemental maps in Fig. 8b).

Mn depletion profiles were also measured in the 120 specimens (EDS elemental profile in Fig. 11). At 800 °C, in both dry and wet air, significant Mn depletion was observed in the center of the foil after 9000–10,000 h, similar to the observed Cr depletion.

For each alloy, the Cr losses due to oxidation and volatilization of the oxide scale were estimated by integrating Cr concentration profiles and by using 8.44 and 8.04 g cm⁻³ as densities for 625 and 120, respectively. For two 120 specimens exposed for 7500 and 9000 h in wet air at 800 °C, the Fe, Cr-rich oxide was observed (Fig. 8) and metal loss was significant (Fig. 10a). Thus, the Cr loss was calculated using the measured thickness of the oxide in Fig. 9b, assuming FeCr_2O_4 stoichiometry and density of 4.97 g cm⁻³. In addition, the obtained Cr losses were normalized (value in %) by dividing each Cr loss by its total initial Cr content in the foil (in mg cm⁻²). Therefore, the evolution of Cr loss is reported in % as a function of time, temperature and environment in Fig. 12. This method allowed Cr loss comparison between the two foils since they did not have identical thicknesses and thus had different initial Cr content. For modeling purposes, the Cr losses will be reported in mg cm⁻² for both 625 and 120 alloys later in the manuscript.

As expected, for both 625 and 120 foils between 625 and 800 °C, larger Cr depletion values were measured in wet air than in dry air (Fig. 12). For the 625 specimen, after 10,000 h exposure in wet air, $2.2 \pm 0.2\%$, $4.9 \pm 0.1\%$, and $15 \pm 2\%$ Cr depletion were measured at 650, 700 and 800 °C. For the 120 specimens, similar Cr depletion ($1.6 \pm 0.4\%$) was measured after 10,000 h at 650 °C, a slightly higher Cr depletion than 625 alloy was measured after 10,000 h at 700 °C ($6.6 \pm 0.1\%$). At 800 °C in both dry and wet air environments, greater Cr depletions were measured for the 120 specimens than for the 625 samples.

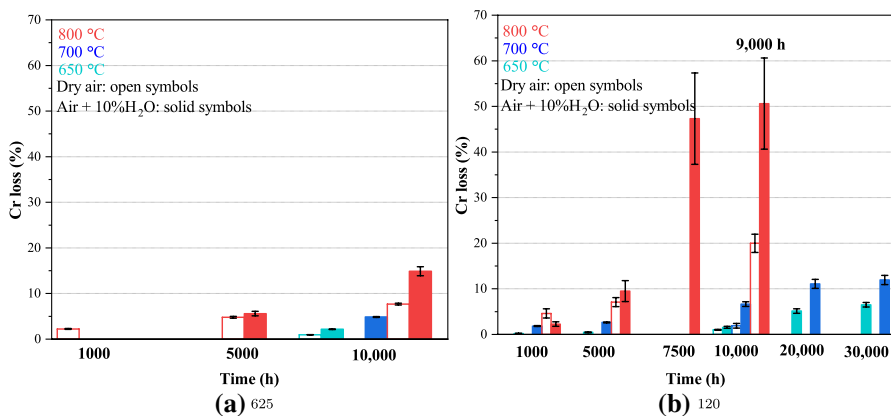


Fig. 12 Evolution of Cr depletion in % as function of time and temperature in **a** 625 and **b** 120 foils exposed in (empty columns) dry air and (colored columns) air + 10% H₂O environments

For example, after 9000 h in wet air at 800 °C, the Cr depletion in 120 specimen was about 3.5 times higher than the Cr depletion in the 625 specimen after 10,000 h exposure ($51 \pm 10\%$ and $15 \pm 2\%$ in 120 and 625, respectively Fig. 12). For the 120 alloy, some Cr depletion values were reported in [39] using a different method with units in wt%. More recently, these values were converted to % in [40] and corresponded to an average of Cr profiles in the matrix and at grain boundaries.

Discussion

Modeling the Effect of Water Vapor on Chromium Loss

The capability of the modeling approach presented in Sect. 3 to predict the Cr loss due to simultaneously occurring oxidation and volatilization processes, using the available thermodynamic data [16, 17], will be evaluated. The calculated and experimental Cr loss values (in mg cm⁻²) for the 625 and 120 specimens are plotted as a function of time and temperature using two different sources for the CrO₂(OH)₂ partial pressures [16, 17] in Fig. 13. In contrast to the previous modeling approaches in [11, 14], the Tedmon's equation [19] was solved numerically to consider concurrent growth and volatilization of the chromia scale in the present study. In both studies [11, 14], it was assumed that the Cr loss was solely governed by the volatilization of the Cr₂O₃ scale.

Very good agreement was obtained between the calculated and experimental Cr loss values in Fig. 13a, for the 625 specimens after 5000 h at 800 °C using data by Gindorf *et al.* [16]. However, the model slightly overestimated Cr loss values with the data by Opila *et al.* [17]. In contrast, a good agreement was obtained with the measured values after 10,000 h using data by Opila *et al.* [17]. For alloy 625, acceptable agreement was obtained between the calculated and experimental Cr loss using

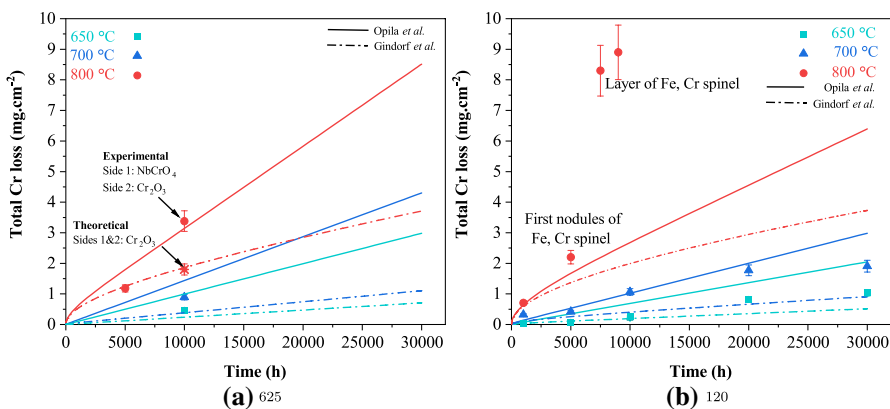


Fig. 13 Experimental and calculated total Cr loss in **a** 625 and **b** 120 specimens after up to 30,000 h between 650 and 800 °C in flowing air + 10% H₂O

data by Gindorf et al. [16] at 650 and 700 °C. However, calculated values were twice higher than the measured values using data measured by Opila et al. [17] for alloy 625 at 650 and 700 °C.

A good agreement was obtained between calculated and experimental Cr loss for the 120 specimens up to 1000 h at 800 °C (Fig. 13b). After 5000 h at 800 °C, the measured Cr loss was higher than the calculated values using both data from Gindorf et al. and Opila et al. [16, 17]. The difference increased with longer exposure times and the measured values were about 2–3 times higher than the calculated ones after 9000 h (Fig. 13b). An acceptable agreement was found between experimental and calculated Cr loss, with the experimental data lying between the two calculated curves for the alloy 120 at 650 and 700 °C (Fig. 13b).

It is important to note that at the lower temperatures of 650 and 700 °C, as mentioned earlier in Sect. 4.1, the oxidation rate constant values were estimated from the steady-state mass change in dry air. As seen in Fig. 1, the mass change values were very small (10^{-2} mg cm⁻²) and close to the balance detection limit (10^{-2} mg cm⁻²). This could affect the estimated oxidation rate constants at these temperatures (as reflected by the coefficient of determination, or R^2 , values, which were 0.74, 0.92 and 1.00 at 650, 700 and 800 °C, respectively). Therefore, it could have resulted in an underestimation of the Cr loss, especially at 650 °C. Another factor that could lead to the underestimation of the oxidation rate constant of the Cr₂O₃ scale is the slightly faster growth in wet air environment [27]. In this study, a factor of about 2 was measured between the oxidation rate constant estimated from the first 100 h of exposure in dry air and wet air at all temperatures. However, doubling the value of the oxidation rate constant in wet air did not significantly affect the observed trends between the calculated and experiment Cr loss values using both thermodynamic data [16, 17] as seen in Fig. 14a and b at 800 °C.

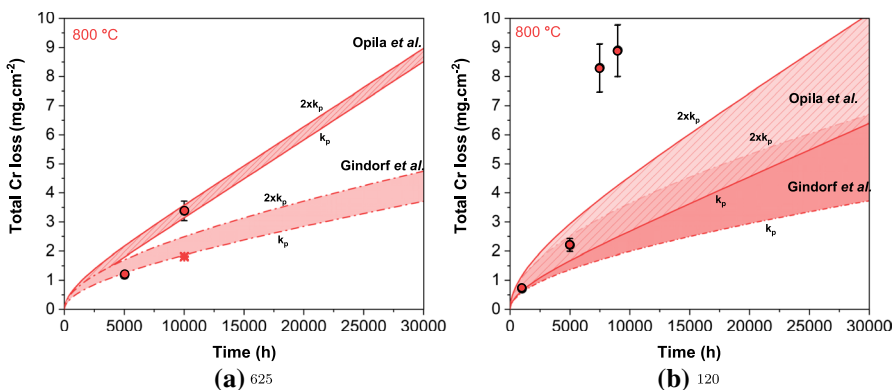


Fig. 14 Experimental and calculated total Cr loss using k_p and twice the value of k_p for **a** 625 and **b** 120 specimens after up to 30,000 h at 800 °C in flowing air + 10% H_2O

In this study, the Cr loss was modeled considering the exclusive growth and volatilization of Cr_2O_3 . This could explain the deviations of calculated Cr loss from measured values, since additional Cr consumed due to the formation and potential volatilization of the Fe and Cr-rich oxides (alloy 120) or the Nb and Cr-rich oxides (alloy 625) is not considered in the model. The implications of the transition from formation of Cr-rich oxide scales to relatively non-protective oxide scales on the oxidation behavior, chromium loss and the modeling results will be discussed in the next section.

Breakdown of Protective Cr-rich Scales and Subsequent Effect on Cr Loss

Nature of Oxides

The breakdown of the Cr_2O_3 was characterized by a steep mass loss for the 625 specimen after 8000 h specimens at 800 °C in air + 10% H_2O (mass change in Fig. 1). The formation of a Cr_2O_3 oxide scale was identified on one side of the specimen whereas on the other side, Nb and Cr-rich mixed oxides were observed to form after 10,000 h (BSE image in Fig. 4b). This specimen also presented an asymmetrical Cr depletion profile (Fig. 10a). The 625 specimen was likely kept in the same position in the alumina boat during the 10,000 h exposure. Therefore, one side of the specimen might have been more exposed to flowing H_2O on the top side than on the bottom side where the gas flow could have been more restricted [40]. At lower temperatures of 650 and 700 °C, the transition between Cr_2O_3 formation into Nb-rich oxide was not observed experimentally within the duration of the experiment (10,000 h) for the 625 foil.

For alloy 625, the formation of a Nb and Cr-rich oxide was induced by the diffusion of Nb towards the alloy-oxide interface [29]. The Cr concentration at the alloy-oxide interface reached a critical value (10 wt% in Fig. 10a) where the Cr_2O_3 oxide scale could no longer be formed in the presence of water vapor. The Nb and Cr-rich oxide was formed on one side of the specimen and more significantly

at the corners due to increased Cr diffusion. These findings were in agreement with the observed breakdown of the Cr_2O_3 into NbCrO_4 spinel oxide on alloy 625 after 1000 h at 900 °C at the leading edge of a 625 coupon in rapidly flowing (600 cm s^{-1}) air + 6% H_2O [14]. A much greater Cr depletion was measured at the specimen corners (a phenomenon referred to as “edge effect” by [41]) and led to the formation of the observed NbCrO_4 spinel oxide. This was also observed for other alloy-environment systems such as FeCrAl exposed up to 2500 h in 100 h cycle dry air [42] or ferritic steels exposed in flowing air + 3% H_2O (27 cm s^{-1}) for 1000 h at 850 °C [43]. In [4], the authors stated that no breakaway oxidation was observed for 625 foil (about 100 μm) after 10,000 h in flowing air + 7% H_2O (0.12 cm s^{-1}) at 815 °C. The calculated total Cr loss rate (oxidation and volatilization), corresponding to this conditions, was 1.5 times higher than in this study at 800 °C. However, in [4], it was not mentioned if other oxides were formed on the surface of the alloy 625 and no

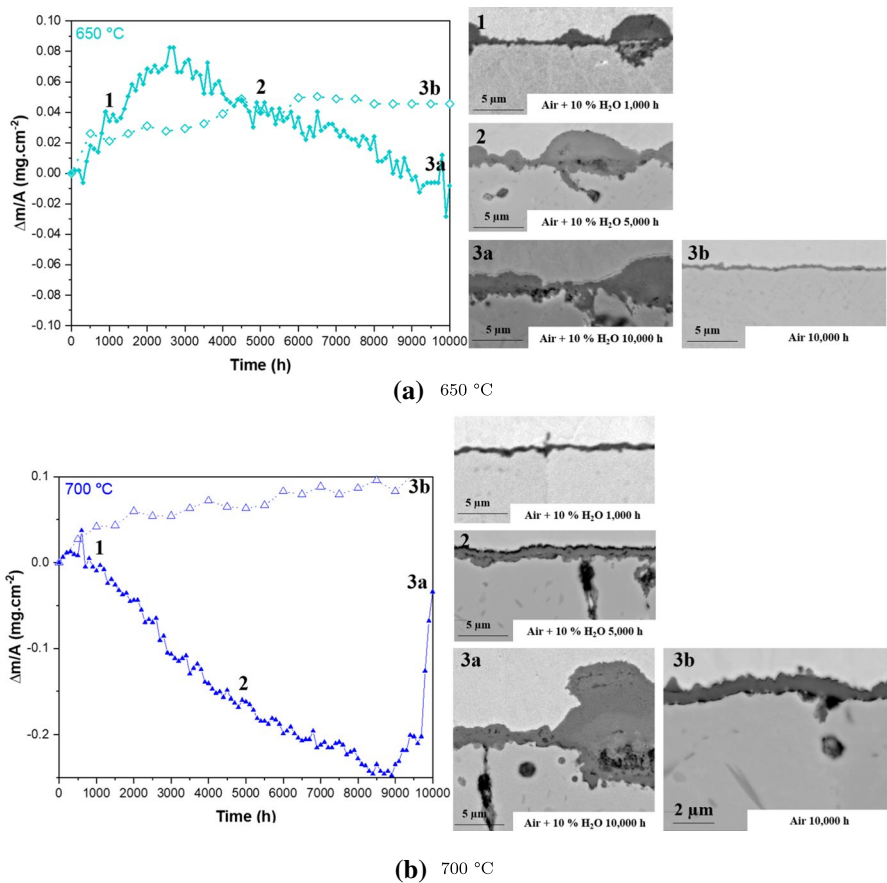


Fig. 15 Mass change as function of time with BSE images of 120 foils after 1000; 5000 and 10,000 h exposure in (open symbols) dry air and (close symbols) air + 10% H_2O at **a** 650 °C and **b** 700 °C

evidence was provided after 10,000 h at 815 °C in flowing air + 7% H₂O (0.12 cm s⁻¹).

The breakdown of the Cr₂O₃ oxide scale was observed after longer exposure times at 700 °C (10,000 h in Figs. 1b and 9b) than at 800 °C (7500 h in Figs. 1b and 9b) for the 120 specimens, in air + 10% H₂O. Cr₂O₃ and MnCr₂O₄ were observed for after 5000 h in both dry and wet air at 700 °C (Fig. 15b). The formation of Fe, Cr mixed oxides was observed after only 1000 h at 650 °C in wet air (Fig. 15a). At this temperature, the Cr transport in the alloy towards the alloy-oxide interface might not have been sufficient to compensate for the Cr loss due to oxidation and volatilization of the Cr₂O₃ scale in contrast to 700 and 800 °C. The Cr₂O₃ breakdown was followed by the formation of fast growing Fe and Cr mixed oxides with underlying Cr₂O₃ (EDS maps in Fig. 8b) at 800 °C in wet air. Similar protective to non-protective oxidation behavior was reported for cold-worked 20Cr–25Ni–Nb/TiN (composition similar to studied alloy 120) strengthened stainless steel coupons exposed in CO₂/1–2%CO containing 300 vppm H₂O and 300 vppm CH₄ between 750 and 900 °C [44]. After 6000 h at 900 °C, the Cr₂O₃ oxide was locally replaced by the rapid growth of (Ni,Fe)₂CrO₄ spinel oxide nodules. The growth of these nodules was later observed to be retarded by the formation of an underlying “healing” Cr₂O₃ layer [45]. In [44], the localized spinel oxide nodules formed were about 30–50 μm which corresponded to about 3% metal loss of the 1.5 mm thick coupons. In the present study, a Cr₂O₃ layer was formed underneath the thick Fe and Cr mixed oxides (Fig. 8b). This layer was 20 ± 5 μm thick on each side of the 81 ± 2 μm foil and corresponded to about 40% metal loss at 800 °C (Fig. 4d). Therefore, the term “healing” layer as used in [44] is not applicable in the present study but could be relevant for thicker specimens.

Effect of Mn

Greater Cr depletions were measured in the 120 foil than for the 625 specimens in both environments (Fig. 12) although the specimens presented relatively similar oxidation rate constants in dry air at 800 °C (oxidation rate constants in Fig. 2). In addition to the higher Fe content in alloy 120, one of the important differences between these alloys is the Mn content. The formation of a MnCr₂O₄ spinel on top of a Cr₂O₃ scale was observed in the literature on the surface of alloy 120 and similar alloys [3, 10, 27, 28, 40, 46, 47]. Specimens with Mn additions were also associated with faster oxidation rate constants [27, 46, 47] and Mn and Cr depletion profiles [46, 47]. The formation of MnCr₂O₄ (Fig. 4), associated with Mn depletion depths equal to the Cr depletion depths in the underlying alloy (Figs. 10 and 11), could be responsible for greater Cr depletion in the 120 specimens than in alloy 625 at 800 °C.

Discrepancies Between Experimental and Modeling Results

A few possible reasons can be identified for the observed deviations between experimental and calculated values. As presented in Sect. 5.1, parameters such as partial pressure and the oxidation constant of the Cr₂O₃ scale were found to affect the discrepancy between the experimental and modeling results. In [14], calculated Cr

losses of alloy 625 were about twice higher than of experimental Cr losses due to Cr_2O_3 volatilization after 1000 h exposure at 900 °C in air + 6% H_2O at two different flow rates 70 cm s⁻¹ and 600 cm s⁻¹ using data by Opila *et al.* [17]. In [11], the calculated Cr losses of 709 foil were also 2–3 times greater than the experimental values after 3000 h at 800 °C in flowing air + 10% H_2O (velocity of 2 cm s⁻¹). In addition, once the alloys begin forming mixed oxides (Fe, Cr-rich scales in case of 120 and Nb, Cr-rich scales on 625), the growth kinetics of these oxides is expected to be faster than that of a pure Cr_2O_3 scale and thus is conjectured with an increased Cr loss. For alloy 625, the calculated Cr loss was in agreement with the measured value after 10,000 h at 800 °C, using data by Opila *et al.* [17], where the Nb, Cr mixed oxides were observed on one side of the foil (Fig. 4b). The measured Cr loss was three times greater than at 5000 h, where Cr_2O_3 was still present on both sides of the foil and in agreement with the Cr loss model using data by Gindorf *et al.* [16] in Fig. 13a. For alloy 120, the measured Cr loss was about 5 times greater after 9000 h than after 5000 h where the oxide scale was mainly Cr_2O_3 . In [11], the Cr loss data for Fe–20Cr–25Ni+Nb (alloy 709) increased between 5000 and 6000 h due to breakaway oxidation (similar to the observation for alloy 120 in this study at longer times) due to the formation of faster growing oxide nodules at 800 °C. This observation could explain why the discrepancy between calculated and measured Cr losses decreased after 6000 h using data by Opila *et al.* [11]. In this study, a time dependent oxidation rate constant would be needed in the Cr loss model to observe good agreement between the experimental values and the model over the entire duration of the experiment. Future work aims to include the transition from the formation of Cr_2O_3 scale to mixed oxides (Nb-rich or Fe, Cr-rich) in the model to include the prediction of t_{10} for both alloys 625 and 120 in dry air and wet air environments as a function of flow rate and foil thickness. The local spallation of the Fe, Cr or Nb, Cr mixed oxides could also be an additional contributor to the total Cr loss. However, the experimental Cr losses were determined from planar surfaces and at locations where spallation did not occur. Foil specimens could also accommodate the stresses created during oxidation by deformation (not shown here). Therefore, the additional Cr loss due to spallation of the Cr_2O_3 before the formation of mixed oxides can be considered minimal.

At 700 °C, although Fe and Cr mixed oxides were formed after 10,000 h in wet air (Figs. 6b and 9) and the Cr loss nearly tripled between 5000 and 30,000 h of exposure (Fig. 12b), the Cr loss did not increase significantly as observed at 800 °C. The potential role of mixed oxides in inhibiting evaporation of chromia scales, as reported in the literature [13, 48, 49] is not considered in the model. To the authors' best knowledge, no value has been reported on the oxidation rate constants of both Nb and Fe, Cr mixed oxides [50] or on the partial pressures of corresponding gaseous species formed after reaction with water vapor.

The earlier breakdown of protective oxidation behavior for 120 in wet air than in dry air suggested limited benefit of the presence of MnCr_2O_4 over a Cr_2O_3 oxide scale on decreasing the Cr_2O_3 volatilization. Breakdown of the duplex layer was observed from the larger mass losses in wet air (after about 5000 h in Fig. 1b) than in dry air (after about 8000 h in Fig. 1b) and the increased Mn depletion in wet air than in dry air in Fig. 11 at 800 °C. Previously, the MnCr_2O_4 formation was

thought to help lower the $\text{CrO}_2(\text{OH})_2$ partial pressure and thus to decrease the metal loss due to Cr_2O_3 volatilization according to the mass transfer theory [49]. More recently [48], using the transpiration method, the Cr vaporization in air + 3% H_2O of Fe–24Cr–0.11Ni–0.19Si (Cr_2O_3 former), was reported to be lower than for Fe–2 2Cr–0.29Ni–0.4Si–0.18Al–0.45Mn and Fe–23Cr–0.4Mn which formed a $(\text{Cr}, \text{Mn})_3\text{O}_4$ layer over a Cr_2O_3 oxide scale after 100 h in flowing (80 ml/min) air + 1.88% H_2O at 800 °C. In [51], a greater volatilization rate of MnCr_2O_4 powder compared to Cr_2O_3 powder was measured after 1000 h exposure in flowing (347 cm/h) air + 10% H_2O between 850 and 1050 °C. Similar Cr losses were observed for alloys 625 (Cr_2O_3 former), 120 and 709 (Cr_2O_3 and MnCr_2O_4 formers) exposed for 10,000 h in water vapor at 650 and 700 °C [40]. The results of the present study provide further evidence to other findings in the literature that the formation of MnCr_2O_4 increases oxidation rates [27, 52] which could negate the potential beneficial effect of the Mn, Cr-spinel on suppressing Cr_2O_3 volatilization.

Summary and Conclusions

The oxidation behavior of 625 and 120 foils was investigated at 650, 700 and 800 °C in dry air and flowing air + 10% H_2O for up to 10,000 h (alloy 625) or 30,000 h (alloy 120). The presence of water vapor in the atmosphere resulted in increased Cr consumption of the foils. The larger Cr depletion in water vapor induced faster loss of protective oxidation behavior.

The Cr loss induced by the coupled oxidation and volatilization behavior of the Cr_2O_3 oxide scale was predicted for the 625 and 120 specimens solving the partial differential equations [25] using mass transfer theory [11, 20]. The influence of $\text{CrO}_2(\text{OH})_2$ partial pressure and the oxidation rate constant on Cr loss values was evaluated. Acceptable agreement was obtained between experimental and calculated Cr loss when the Cr_2O_3 oxide scale was sustained. The growth and volatilization of the Fe, Cr-rich and Nb, Cr-rich oxides was not implemented in the model and led to underestimations of the Cr loss after breakdown of the oxide scale at 800 °C. At this temperature, the loss of protective oxidation behavior was observed after a shorter duration for alloy 120 than for alloy 625. Larger Cr depletions were observed for the 120 specimen than for 625 specimen despite the formation of MnCr_2O_4 on top of a Cr_2O_3 oxide layer indicating that the MnCr_2O_4 product did not attenuate further Cr_2O_3 volatilization in the wet atmosphere. In addition, the presence of 32%Fe in alloy 120 led to the formation of a thick Fe and Cr-rich oxide layer and an underlying thin Cr_2O_3 layer which resulted in almost 50% Cr loss after 5000 h exposure at 800 °C in wet air. For the 625 specimen, the Cr_2O_3 breakdown occurred on one side of the foil and at the corners. The presence and enrichment of Nb at the alloy-oxide interface resulted in the formation of Nb-rich oxide and 15% Cr loss. In addition, the effect of the mixed oxide formation on the Cr loss was discussed in terms of initial foil thickness. In the case of the 80 μm thick alloy 120 foil, the formation of the Fe, Cr-rich oxide at 800 °C consumed half of the Cr reservoir in about 10,000 h in wet air but the effect would be reduced for thick-walled components.

At 650 and 700 °C in wet air, the differences in oxide scale nature (Cr_2O_3 for alloy 625, Cr_2O_3 and MnCr_2O_4 followed by their breakdown into Fe and Cr-rich oxide with underlying Cr_2O_3 for alloy 120) resulted in comparable Cr losses after 10,000 h. At these temperatures, good agreement was obtained between the calculated and experimental Cr values up to 30,000 h for alloy 120 and 10,000 h for alloy 625 independent of the value of the $\text{CrO}_2(\text{OH})_2$ partial pressure and oxidation rate constant.

Acknowledgements The author would like to thank G. W. Garner, M. S. Stephens, T. Lowe, V. Cox at ORNL for their assistance with the experimental work and P. F. Tortorelli and M. Brady for their valuable comments on the manuscript. This research was sponsored by the U. S. Department of Energy, Office of Energy Efficiency and Renewable Energy, Combined Heat and Power Program.

References

1. C. F. McDonald, *Applied Thermal Engineering* **23**, 1463 (2003). [https://doi.org/10.1016/S1359-4311\(03\)00083-8](https://doi.org/10.1016/S1359-4311(03)00083-8).
2. P. Maziasz, R. Swindeman, J. Shingledecker, K. More, B. Pint, E. Lara-Curzio and N. Evans, *Book- Institute of Materials* **800**, 1057 (2003).
3. B. A. Pint, *Journal of Engineering for Gas Turbines and Power* **128**, 370 (2004). <https://doi.org/10.1115/1.2056531>.
4. J. M. Rakowski, C. P. Stinner, M. Lipschutz and J. P. Montague, The use and performance of wrought 625 alloy in primary surface recuperators for gas turbine engines, in: Proceedings of Superalloys 718, p. 625 (2005).
5. M. D. Bender and R. C. Klug, Comparison of Ni-based 625 alloy and ATI 20-25+NbTM stainless steel foils after long-term exposure to gas turbine engine exhaust, in: Proceedings of the ASME Turbo Expo, vol. GT2014-25334 (2014). <https://doi.org/10.1115/GT2014-25334>.
6. J. Ehlers, D. J. Young, E. J. Smaardijk, A. K. Tyagi, H. J. Penkalla, L. Singheiser and W. J. Quadakkers, *Corrosion Science* **48**, 3428 (2006). <https://doi.org/10.1016/j.corsci.2006.02.002>.
7. W.J. Quadakkers, J. Zurek and M. Hänsel, *JOM* **61**, 44 (2009). <https://doi.org/10.1007/s11837-009-0102-y>.
8. H. Asteman, J. E. Svensson, L. G. Johansson and M. Norell, *Oxidation of Metals* **52**, 95 (1999). <https://doi.org/10.1023/a:1018875024306>.
9. R. Peraldi and B. A. Pint, *Oxidation of Metals* **61**, 463 (2004).
10. B. A. Pint, The effect of water vapor on Cr depletion in advanced recuperator alloys, in: Turbo Expo: Power for Land, Sea, and Air, vol. 46997, p. 927 (2005).
11. D. J. Young and B. A. Pint, *Oxidation of Metals* **66**, 137 (2006). <https://doi.org/10.1007/s11085-006-9030-1>.
12. B. A. Pint, K. L. More, R. M. Trejo and E. Lara-Curzio, *Journal of Engineering for Gas Turbines and Power* **130**. <https://doi.org/10.1115/GT2006-90194>.
13. T. Sand, C. Geers, Y. Cao, J. E. Svensson and L. G. Johansson, *Oxidation of Metals* **92**, 259 (2019). <https://doi.org/10.1007/s11085-019-09935-9>.
14. P. Huczkowski, W. Lehnert, H. H. Angermann, A. Chyrkin, R. Pillai, D. Grüner, E. Hejrani and W. J. Quadakkers, *Materials and Corrosion* **68**, 159 (2017). <https://doi.org/10.1002/maco.201608831>.
15. R. Pillai, S. Dryepondt and B. A. Pint, High temperature oxidation lifetime modeling of thin-walled components, in: ASME Turbo Expo Volume 6: Ceramics; Controls, Diagnostics, and Instrumentation; Education; Manufacturing Materials and Metallurgy, Phoenix, Arizona, USA, June 17–21, 2019, p. 1 (2019).
16. C. Gindorf, L. Singheiser and K. Hilpert, *Journal of Physics and Chemistry of Solids* **66**, 384 (2005). <https://doi.org/10.1016/j.jpcs.2004.06.092>.
17. E. J. Opila, D. L. Myers, N. S. Jacobson, I. M. B. Nielsen, D. F. Johnson, J. K. Olminsky and M. D. Allendorf, *Journal of Physical Chemistry A* **111**, 1971 (2007). <https://doi.org/10.1021/jp0647380>.
18. B. A. Pint, K. L. More, R. M. Trejo and E. Lara-Curzio, *Journal of Engineering for Gas Turbines and Power-Transactions of the ASME* **130**, 271 (2008). <https://doi.org/10.1115/1.2436565>.
19. C. Tedmon, *Journal of the Electrochemical Society* **113**, 3 (1966).
20. G. R. Holcomb, *Oxidation of Metals* **69**, 163 (2008). <https://doi.org/10.1007/s11085-008-9091-4>.

21. G. R. Holcomb, *Journal of the Electrochemical Society* **156**, C292 (2009). <https://doi.org/10.1149/1.3155442>.
22. B. B. Ebbinghaus, *Combustion and Flame* **93**, 119 (1993). [https://doi.org/10.1016/0010-2180\(93\)90087-J](https://doi.org/10.1016/0010-2180(93)90087-J).
23. V. P. Deodeshmukh, *Oxidation of Metals* **79**, 567 (2013). <https://doi.org/10.1007/s11085-012-9343-1>.
24. V. P. Deodeshmukh, *Oxidation of Metals* **79**, 579 (2013). <https://doi.org/10.1007/s11085-012-9344-0>.
25. C. A. Barrett and A. Presler, COREST: A FORTRAN computer program to analyze paralinear oxidation behavior and its application to chromic oxide forming alloys, Report NASA-TN-D-8132, E-8432, NASA Lewis Research Center; Cleveland, OH, United States (1976).
26. MATLAB, R2019b, The MathWorks Inc., Natick, Massachusetts (2019).
27. J. Zurek, D. Young, E. Essuman, M. Hänsel, H. J. Penkalla, L. Niewolak, and W. J. Quadakkers, *Materials Science and Engineering: A* **477**, 259 (2008). <https://doi.org/10.1016/j.msea.2007.05.035>.
28. X. Ledoux, S. Mathieu, M. Vilasi, Y. Wouters, P. Del-Gallo and M. Wagner, *Oxidation of Metals* **80**, 25 (2013). <https://doi.org/10.1007/s11085-013-9367-1>.
29. A. Chyrkin, P. Huczowski, V. Shemet, L. Singheiser and W. J. Quadakkers, *Oxidation of Metals* **75**, 143 (2011). <https://doi.org/10.1007/s11085-010-9225-3>.
30. N. Ramenat, A. Vernouillet, S. Mathieu, A. Vande Put, M. Vilasi and D. Monceau, *Corrosion Science* **164**, 108347 (2020). <https://doi.org/10.1016/j.corsci.2019.108347>. <https://www.sciencedirect.com/science/article/pii/S0010938X19314556>.
31. J. Colas, L. Charpentier and M. Balat-Pichelin, *Oxidation of Metals* **93**, 355 (2020). doi: 10.1007/s11085-020-09959-6.
32. H. Buscail, R. Rolland, C. Issartel, F. Rabaste, F. Riffard, L. Aranda and M. Vilasi, *Journal of Materials Science* **46**, 5903 (2011). doi: 10.1007/s10853-011-5544-2.
33. P. J. Maziasz, B. A. Pint, J. P. Shingledecker, N. D. Evans, Y. Yamamoto, K. L. More and E. Lara-Curcio, *International Journal of Hydrogen Energy* **32**, 3622 (2007). doi: 10.1016/j.ijhydene.2006.08.018.
34. P. J. Maziasz, J. P. Shingledecker, B. A. Pint, N. D. Evans, Y. Yamamoto, K. More and E. Lara-Curcio, *Journal of Turbomachinery-Transactions of the ASME* **128**, 814 (2006).
35. M. D. Mathew, P. Parameswaran and K. Bhanu Sankara Rao, *Materials Characterization* **59**, 508 (2008). <https://doi.org/10.1016/j.matchar.2007.03.007>.
36. J. E. Croll and G. R. Wallwork, *Oxidation of Metals* **1**, 55 (1969). <https://doi.org/10.1007/BF00609924>.
37. R. Pillai, H. Ackermann and K. Lucka, *Corrosion Science* **69**, 181 (2013). <https://doi.org/10.1016/j.corsci.2012.11.040>.
38. R. Duan, A. Jalowicka, K. Unocic, B. A. Pint, P. Huczowski, A. Chyrkin, D. Grüner, R. Pillai and W. J. Quadakkers, *Oxidation of Metals* **87**, 11 (2017). <https://doi.org/10.1007/s11085-016-9653-9>.
39. B. Pint, S. Dryepondt, A. Rouaix-Vande Put and Y. Zhang, *Journal of the Minerals Metals and Materials Society (JOM)* **64**. <https://doi.org/10.1007/s11837-012-0474-2>.
40. B. A. Pint, Addressing the Role of Water Vapor on Long-term Stainless Steel Oxidation Behavior. Oxidation of Metals (in Press).
41. W. M. Pragnell and H. E. Evans, *Oxidation of Metals* **66**, 209 (2006). <https://doi.org/10.1007/s11085-006-9039-5>.
42. I. Wright, R. Peraldi and B. Pint, *Materials Science Forum - MATER SCI FORUM* **461–464**, 579 (2004). <https://doi.org/10.4028/www.scientific.net/MSF.461-464.579>.
43. R. Sachitanand, J. E. Svensson and J. Froitzheim, *Oxidation of Metals* **84**, 241 (2015). <https://doi.org/10.1007/s11085-015-9552-5>.
44. H. E. Evans, D. A. Hilton, R. A. Holm and S. J. Webster, *Oxidation of Metals* **14**, 235 (1980). <https://doi.org/10.1007/BF00604566>.
45. R. C. Lobb and H. E. Evans, *Corrosion Science* **24**, 385 (1984). [https://doi.org/10.1016/0010-938X\(84\)90065-9](https://doi.org/10.1016/0010-938X(84)90065-9).
46. T. Perez, L. Latu-Romain, R. Podor, J. Lautru, Y. Parsa, S. Mathieu, M. Vilasi and Y. Wouters, *Oxidation of Metals* **89**, 781 (2017).
47. M. Romedenne, R. Pillai, M. Kirka and S. Dryepondt, *Corrosion Science* **171**, 108647 (2020). <https://doi.org/10.1016/j.corsci.2020.108647>.
48. M. Stanislowski, J. Froitzheim, L. Niewolak, W. J. Quadakkers, K. Hilpert, T. Markus and L. Singheiser, *Journal of Power Sources* **164**, 578 (2007).
49. G. R. Holcomb and D. E. Alman, *Journal of Materials Engineering and Performance* **15**, 394 (2006). <https://doi.org/10.1361/105994906X117170>.
50. J. E. Croll and G. R. Wallwork, *Oxidation of Metals* **4**, 121 (1972). <https://doi.org/10.1007/Bf00613088>.

51. A. Stenzel, D. Fahsing, M. Schutze and M. C. Galetz, *Materials and Corrosion-Werkstoffe Und Korrosion* **70**, 1426 (2019). <https://doi.org/10.1002/maco.201810655>.
52. D. L. Douglass and J. S. Armijo, *Oxidation of Metals* **2**, 207 (1970). <https://doi.org/10.1007/BF00603657>.

Publisher's Note Springer Nature remains neutral with regard to jurisdictional claims in published maps and institutional affiliations.